Automatic myocardial ischemic lesion detection on magnetic resonance perfusion weighted imaging prior perfusion quantification: A pre-modeling strategy

Clément Daviller, Thomas Grenier, Hélène Ratiney, Michaël Sdika, Pierre Croisille, Magalie Viallon

Automatic Myocardial Ischemic Lesion Detection on Magnetic Resonance Perfusion Weighted Imaging prior Perfusion Quantification: a pre-modeling strategy.

Clément Daviller[1], Thomas Grenier[1], Helene Ratiney[1], Michaël Sdika[1], Pierre Croisille[2,3] and Magalie Viallon[2,3]

1. Univ. Lyon, INSA-Lyon, Université Claude Bernard Lyon 1, UJM-Saint Etienne, CNRS, Inserm, CREATIS UMR 5520, U1206, F-69621, VILLEURBANNE, France

2. Univ Lyon, UJM-Saint-Etienne, INSA, CNRS UMR 5520, INSERM U1206, CREATIS, F-42023, SAINT-ETIENNE, France

3. Radiology Dept. CHU de Saint Etienne, Univ Lyon, UJM-Saint-Etienne, F-42023, SAINT-ETIENNE, France

Corresponding author : Clément Daviller

Mail : clement.daviller@creatis.insa-lyon.fr

Phone : +33 (0)4 72 44 80 15 fax: +33 (0)4 72 44 81 99

Address: 3, rue Victor Grignard 69616 Villeurbanne Cedex France

Abstract

Even if cardiovascular magnetic resonance (CMR) perfusion imaging has proven its relevance for visual detection of ischemia, myocardial blood flow (MBF) quantification at the voxel observation scale remains challenging. Integration of an automated segmentation step, prior to perfusion index estimation, might be a significant reconstruction component that could allow sustainable assumptions and constraint enlargement prior to advanced modeling. Current clustering techniques, such as bullseye representation or manual delineation, are not designed to discriminate voxels belonging to the lesion from healthy areas. Hence, the resulting average time–intensity curve, which is assumed to represent the dynamic contrast enhancement inside of a lesion, might be contaminated by voxels with perfectly healthy microcirculation.

This study introduces a hierarchical lesion segmentation approach based on time–intensity curve features that considers the spatial particularities of CMR myocardial perfusion. A first k-means clustering approach enables this method to perform coarse clustering, which is refined by a novel spatiotemporal region-growing (STRG) segmentation, thus ensuring spatial and time–intensity curve homogeneity.

Over a cohort of 30 patients, myocardial blood flow (MBF) measured in voxels of lesion regions detected with STRG was significantly lower than in regions drawn manually (mean difference = 0.14, 95% CI [0.07, 0.2]) and defined with the bullseye template (mean difference = 0.25, 95% CI [0.17, 0.36]). Over the 90 analyzed slices, he median Dice scores calculated against the ground truth ranged between 0.62 and 0.67, the inclusion coefficients ranged between 0.62 and 0.76 and the centroid distances ranged between 0.97 3.88 mm. Therefore, though these metrics highlight spatial differences, they could not be used as an index to evaluate the accuracy and performance of the method, which can only be attested by the variability of the MBF clinical index.

Introduction

MR contrast-enhanced myocardial perfusion imaging (ceMPI) can supply insight into microcirculation in myocardial tissue[1]. In coronary artery disease (CAD), this method offers crucial information on the impact of vessel lesions with flow reduction. ceMPI also allows myocardial blood flow assessment, topics that are of major interest in CAD lesion detection and clinical decisions. Numerous studies have further demonstrated the ability to quantify myocardial perfusion from MR perfusion-weighted (PW) image series [2,3].

However, although quantitative perfusion indexes such as myocardial blood flow (MBF) have proven their usefulness for diagnosis [4,5], they remain rare in clinical use. Among the obstacles that must be overcome are (i) the complexity of the protocol from PW image acquisition to quantification, (ii) the wide variability between results produced by the approaches, (iii) the large amount of data that must be processed, and (iv) the numerous assumptions that must be met to reduce the number of solutions because deconvolution is an ill-posed inverse problem.

Quantitative measurement approaches are usually divided into two categories: model independent and parametric approaches. Model-independent approaches assume the myocardial circulation system is linear and shift invariant (LSI) [2]. These approaches are often preferred but are noise sensitive because the introduction of small input errors might result in large measurement bias [6]. Large measurement biases particularly occur in regions with perfusion defects where the contrast-to-noise ratio (CNR) is poor due to low signal enhancement of the time-intensity curves. In contrast, model-dependent approaches rely on parametric determination of the residue function R(t) and are constructed with various levels of complexity [7]. Despite their theoretical accuracy, numerous assumptions must be satisfied prior to measurement that are often not sustainable and cannot be made at the voxel level in a reasonable amount of time.

For these reasons, observation at a higher scale than the voxel is often preferred. Among the alternative methods are manual segmentation of lesions or the use of the American Heart Association (AHA) bullseye template, in which the myocardium regions are assigned to 17 predetermined anatomical segments [8]. Manual segmentation requires that the boundary lesion delineation be left to the clinician, which is time-consuming and subjective due to operator dependence. If the AHA bullseye template method is rapid and sufficient in the supply of a semiquantitative coarse overview of the lesion extent in clinical summary reports, it is actually not an acceptable template for quantification. Indeed, the AHA theoretical anatomical boundaries rarely match the individual lesion shapes. This approximation can lead to a nearly

systematic over- or underestimation bias of the perfusion index, measurements depending on the perfusion level of the contaminating tissue.

Recently, promising segmentation methods [9,10] have been proposed that locally cluster the voxels based on quantitative perfusion index similarity. However, even if these techniques supply segmentation that considers the shape of the suffering territory, the segmentation is conducted after the quantification.

In this work, we propose a new segmentation method based on spatiotemporal region growing which clusters the neighboring myocardium voxels with similar tissue characteristics. This approach is based on temporal signal behavior that is wisely conditioned by lesion-specific features. Therefore, a first contribution is the extraction of the classically used lesion-specific features in a more robust way.

The performance of our unsupervised boundary lesion delineation was evaluated by i) comparing the MBF values calculated in the obtained classified regions against these extracted from expert segmentation, over a cohort of 30 subjects referred for known or suspected CAD for a perfusion CMR with pharmacological stress in clinical settings and ii) comparing the ROIs obtained by our unsupervised technique and ROIs defined by expert segmentation by calculating the Dice score inclusion coefficient and the centroid distance.

Materials and methods

Study population and MR Acquisition

We recruited thirty patients referred for known or suspected CAD with perfusion CMR. The study was performed with the approval of the Institutional Review Board (IRBN 052019/ CHUSTE), and written informed consent was obtained from all subjects. We excluded patients if they had metallic implants or implanted cardiac devices incompatible with CMR, a glomerular filtration rate ≤ 30 ml/min, a high degree of atrioventricular (AV) blocks, severe chronic obstructive pulmonary disease, or claustrophobia. Patients were asked to abstain from caffeine-containing products for ≥ 12 hours prior to CMR examination.

Perfusion imaging was performed using a dual-acquisition approach as described by Gatehouse et al. [11], on a 3 T MAGNETOM PRISMA scanner (Siemens Healthineers, Erlangen, Germany) with an 18-element surface coil. A standard protocol was used with cardiac localization, steady-state free-precession cine images acquired to cover the heart from base to apex. Contrast-enhanced inversion-recovery images were acquired 10 min after

injection. Vasodilation was obtained with a 0.4 ml bolus injection of Regadenoson (Rapiscan, GEMS) 1 minute before imaging. Perfusion acquisition was subsequently performed at 3 to 5 short-axis locations at every heart beat with a bolus injection (6 ml/s) of gadoterate meglumine (0.2 mmol/kg) (Dotarem, France). We used the first 10 interbeat RR intervals for precontrast baseline signal measurement, and the data were acquired in free-breathing mode 60 to 110 heartbeats (~60-70 s). Two types of images were acquired at every heart beat: i) a saturation recovery (SR)-prepared sequence with low resolution and a short-recovery-time (LR-SRT) image to avoid saturation of the LV-blood pool signal, and ii) SR-prepared with fine resolution and long-recovery-time (FR-LRT) images for 3 to 5 slices that could fit into the RR interval. The LR-SRT image series was used in arterial input function AIF estimation, and the FR-LRT series were used in perfusion analysis. The sequence acquired the first 3 proton density (PD)-weighted scans planned for signal spatial normalization (flip angle 5°) before imaging of the T1-weighted frames. T1 weighting was obtained with a nonselective SR pulse train followed by a saturation recovery time, defined as the duration between the end of the saturation pulse and the beginning of k-space acquisition. The acquisition kernel was a 2D single-shot turbo-Flash sequence. The FR-LRT main acquisition parameters were assigned as follows: spatial resolution = 1.98 × 1.98 mm², long saturation-recovery time = 43 ms, flip angle α = 10°, TR = 2ms, echo time TE = 0.95 ms, parallel acquisition (TPAT) mode using generalized autocalibrating partially parallel acquisitions (GRAPPA) with acceleration factor = 3, and linear k-space reordering. The LR-SRT images main MR parameters were: spatial resolution = 5.94 × 5.94 mm², flip angle α = 8°, repetition time TR = 1.3 ms, echo time TE = 0.74 ms, short saturation recovery time = 5 ms, centric k-space reordering. For both acquisitions, slice thickness = 8 mm, FOV = 380×380 mm^2.

Data analysis

This section details the proposed data processing, which is summarized in figure 1. In the following, we denote an image series as the time-intensity curves $c_i(t)$ of each voxel v_i.

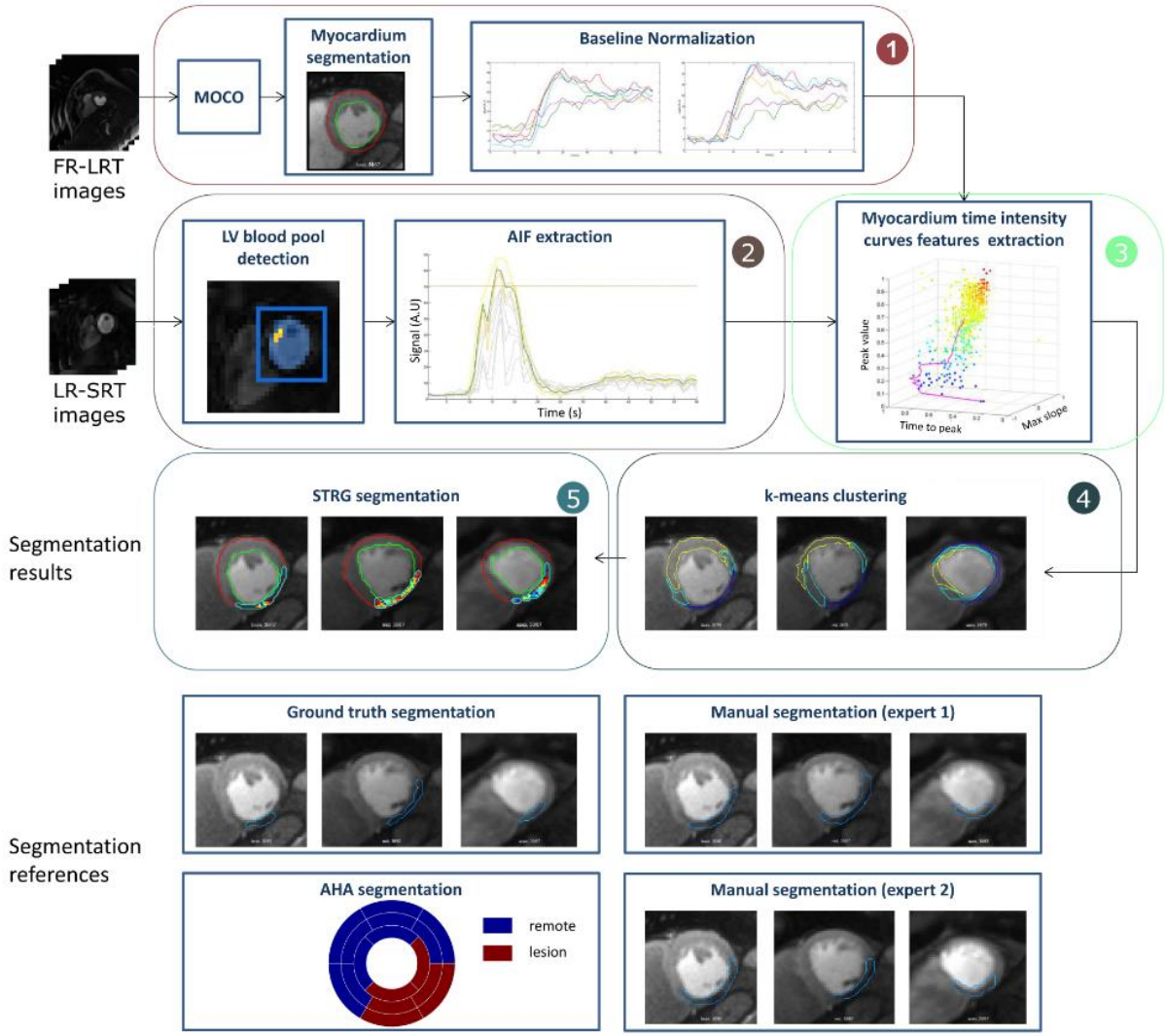

Figure 1: *Global overview of the proposed pipeline for the myocardium segmentation process. Inputs of the pipeline are the low-resolution short-recovery-time (LR-SRT) and fine resolution long-recovery-time (FR-LRT) image series. The steps described in the Materials and methods are numbered here by the bullet points from 1 to 5. Both series types are processed independently (step 1 and 2) to extract myocardium time intensity curve features (step 3). These features are exploited to process the segmentation approach composed of a first coarse k-means clustering (step 4), allowing myocardium lesion location. It is followed by spatio temporal region-growing (STRG) segmentation refinement giving a precise contour of the lesion (step 5). The results are finally compared to reference segmentations performed by two experts. The ground-truth segmentation is the result of their consensus of what they considered as definite ischemic lesion.*

Step 1: Preprocessing of MOCO, normalization and manual myocardial segmentation

First, all MR images (LR-SRT and FR-LRT) were normalized and motion corrected by the non-rigid Siemens MOCO algorithm [12], as reported in Figure 1. For each slice level, LV myocardium segmentation was manually performed by drawing the endo- and epicardial contours on the temporal-maximal-intensity-projection (tMIP) image [10,13]. This image was enhanced with an emphasis filter to sharpen the myocardium borders. This image clearly delineated the endo- and epicardial contours, especially by highlighting the left and right ventricle cavities, as well as the LV lateral portion of the myocardial wall. We applied the same myocardium segmentation template for all analyses.

Step 2: Estimating AIF to improve feature extraction

Most of the approaches that address myocardial lesion segmentation [14] or analysis are based on the features extracted from FR-LRT: peak value, time to peak, maximum upslope, area under the curve, contrast agent bolus arrival delay, etc. These features might not be robustly extracted from the image series because artifacts, noise, movement correction errors or normalization bias can occur in a clinical acquisition context. Therefore, we attempted to improve the feature extraction using assumptions based on AIF knowledge.

We first estimated the AIF from the LR-SRT images to avoid signal distortions. On these images, the blood pool was detected first. From this detection, the curve with the maximum peak intensity value $C_{max}(t)$ served as a reference to aggregate other voxels, with $c_i(t)$ reaching 80% of this maximum value(see appendix A1). Finally, all of the curves were averaged to compute the mean AIF time-intensity curve $S_a(t)$

Subsequently, we extracted the following features from $S_a(t)$:

- peak value P_a, as the maximum value reached by S_a (t)
- peak date t_{Pa}, as the time required for S_a to reach P_a
- foot $t_{Fa,}$ as the time required for S_a to reach 5% of P_a before reaching P_a
- AIF first pass end date $t_{Ea,}$ as the minimum signal intensity value reached by S_a after t_{Pa} and before the recirculation peak.

Step 3: Robust tissue features extraction for improved segmentation

As described in step 2, robust segmentation relies on features that are wisely extracted from the myocardium tissue time-intensity curves $S_m(t)$. Indeed, the robustness and accuracy of the segmentation method described in this article rely on these features. A high contrast-to-noise ratio (CNR) of $S_a(t)$ makes AIF features extraction easy. However, myocardium time-intensity

curves $S_m(t)$ with lower CNR and more exposure to artifacts require more complex processing to yield accurate feature extraction. In the following section, we propose a new lesion specific feature extraction method that is more robust to artifacts. We combine the prior knowledge of the $S_a(t)$ features with two assumptions. First, the studied system is causal. As a consequence, myocardium signal enhancement cannot start before t_{Fa}. Second, we consider that the $S_m(t)$ peak value cannot occur after the end of the AIF first pass. These latter values are set as hierarchical constraints for search of $S_m(t)$ features of voxels present in the myocardium region (manually delineated) extracted from the FR-LRT images in manner similar to AIF estimation:

- The peak value P_m in the tissue is calculated as the maximum value of $S_m(t)$ with t ranging from the AIF foot and the end of the AIF first pass (equation 1)

$$P_m = \max_{t \in [t_{Pa};\, t_{Ea}]} (S_m(t)) \quad (1)$$

- The peak date t_{Pm} is the time required for $S_m(t)$ to reach P_m
- The area under the curve AUC is calculated as the sum of the $S_m(t)$ values (equation 2)

$$AUC = \sum_{t=0}^{t_{Pm}} |S_m(t)| \quad (2)$$

- The $S_m(t)$ foot t_{Fm} is calculated in the same way as t_{Fa}
- The bolus arrival delay Δt_{Fm} is calculated as the time difference between t_{Fa} and t_{Fm} (equation 3)

$$\Delta t_{Fm} = t_{F_m} - t_{Fa} \quad (3)$$

- The maximum upslope is calculated as the maximum intensity difference in a time interval Δt between two consecutive acquisitions in the time range from t_{Fm} to t_{Pm} (equation 4)

$$\delta_{max} = \max_{t \in [t_{Fm};\, t_{Pm}]} (S_m(t + \Delta t) - S_m(t)) \quad (4)$$

- The time to peak Δt_{max} is the time difference between t_{Fm} and t_{Pm} (equation 5)

$$\Delta t_{max} = t_{Pm} - t_{Fm} \quad (5)$$

This hierarchical approach avoids feature computation errors due to noise and variability of the time-intensity curve shapes and supplies robust material for the following lesion detection step. In the following segmentation approach, the 4 features P_m, δ_{max}, AUC and Δt_{max} are used.

Figure 2 presents a 3-dimensional space representation of the features extracted from the time-intensity curves in the PW images acquired on a patient suffering from a severe stenosis. The three dimensions are the usual perfusion semi quantitative parameters: maximum slope δ_{max}, peak value P_m and time to peak Δt_{max}. This plot gives a simple visualization of the differences between the time-intensity curve features from the affected regions and from remote tissue.

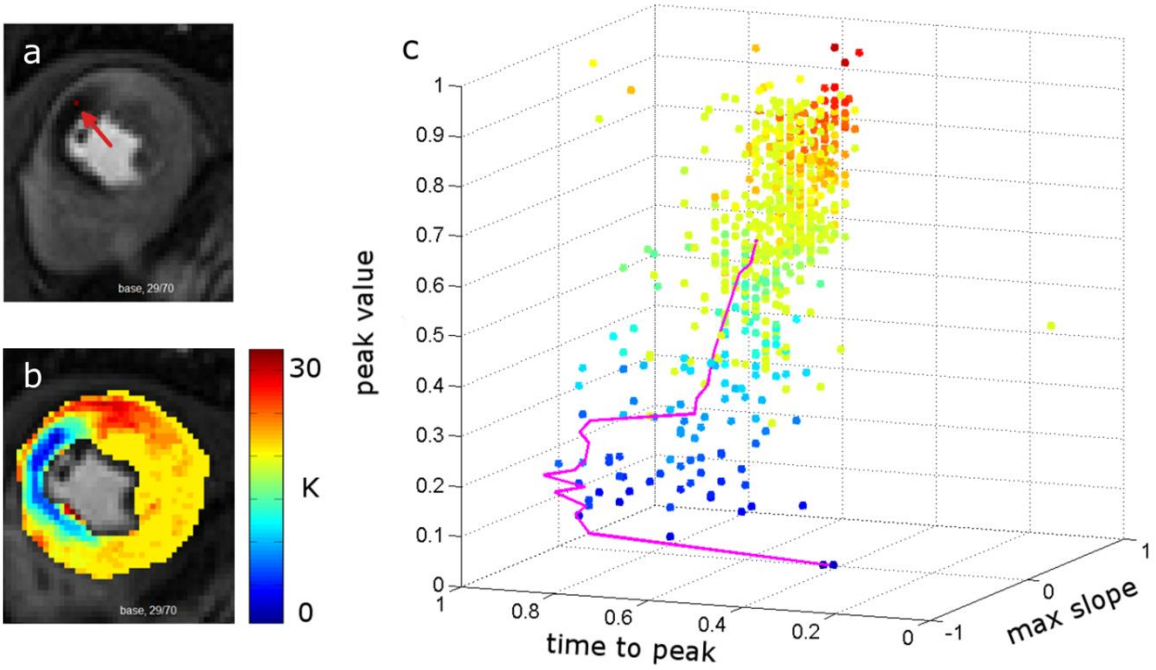

Figure 2: *Extraction of myocardium voxels' time-intensity curve features (peak value, time to peak and maximum slope). The extraction starts from the voxel seed (red voxel in a.) with the lowest area under the curve and considered the center of the lesion. The seed is iteratively expanded to its neighbors, according to equation 9. At each iteration, the tolerance threshold K is incremented until covering the entire myocardium. The map on (b) represents the minimum value of K required to include a voxel in the region. (c) Time-intensity curve features of each voxel are displayed in the 3D feature space. Color map of the points is identical to (b). The magenta curve in (c) represents the region-growing scheme of the average time-intensity curve feature evolution of the growing region as a function of the iteration.*

Step 4: Segmentation based on K-means clustering

From the features P_m, δ_{max}, AUC and Δt_{max} extracted from the voxels in the myocardial region and for each slice, a first coarse clustering pass was applied using the k-means [15] algorithm. The choice of k-means was motivated by the fact that only one parameter is needed by this simple and well used method for segmentation problems. The principle of this unsupervised approach is briefly reviewed.

The aim is to cluster the myocardium voxels v_i into a defined number of clusters *k*. Each voxel v_i is associated with a vector of feature values φ_i. k-means clustering consists of minimizing the vector distance of voxels within a cluster by iteratively moving μ_j (equation 6):

$$\min \sum_{j=1}^{k} \sum_{\varphi_i \in C_j} \left\| \varphi_i - \mu_j \right\|^2 \qquad (6)$$

where *j* is the cluster index, i is the voxel vector index number, φ_i and μ_j are respectively the feature vectors [P_m, δ_{max}, AUC, Δt_{max}] of voxel *i* and cluster centroid *j*, and C_j is the set of voxels associated with cluster *j* (a voxel φ_i is associated with its closer C_j according to the Euclidean distance).

This minimization is performed by k-means based on the algorithm proposed by Arthur and Vassilvitskii [16], which improves the running time and the overall quality of the final solution.

Based on physiological considerations, the number of clusters k was set to 3, assuming that a gradient exists in the voxel features from the healthy tissue areas to the affected tissue areas. The third cluster gathers voxels with maximal time-intensity curve features, and the second gathers voxels with gradual time-intensity curve enhancement. The first cluster is composed of voxels with the poorest enhancement features.

Voxels v_i belonging to the first cluster C_1 (i.e., the voxels cluster with the lower average time-intensity curve sum) are considered abnormal perfusion areas and are reported in a 2-dimensional mask *R*. This mask R is finally set as an input of a connected component analysis to identify possible multiple lesion regions labeled R_n in the myocardium, where all 8-connexity connected voxels v_i reported in R are labeled with an identical value. This rule can be described by equation 7:

$$R = C_1 = \bigcup_n R_n \qquad (7)$$

Step 5: Myocardial lesion segmentation refinement using spatiotemporal region growing (STRG)

This step details our major methodological contribution: the STRG algorithm is applied on each labeled region R_n outputted by the k-means clustering described in step 4. The principle of this approach is to expand a seed defined as the voxel with the lowest time-intensity curve sum, as defined by equation 8:

$$v_{seed,n} = \underset{v \in Rn}{\arg\min} \sum_{t=0}^{T} C_v(t) \quad (8)$$

where n is the index of the labeled region R_n, and T is the last acquisition of the time series.

The region R_n is expanded on its 12 connected neighbors (Figure 3-a) belonging to R_n, and matching the condition set by equation 9:

$$\left\| C_i(t) - C_{seed,Rn}(t) \right\|_\infty \leq K, with\ i\ such\ as\ v_i \in N_{12}(R_n) \quad (9)$$

We note that each v_i is the time-intensity curve $C_i(t)$ and that $\|\cdot\|_\infty$ represents the infinity norm, meaning that we retain the maximum difference between $C_i(t)$ and $C_{seed,Rn}(t)$. In other words, at each acquisition the intensity difference between the current analyzed voxel v_i and the seed must be lower than a tolerance threshold K.

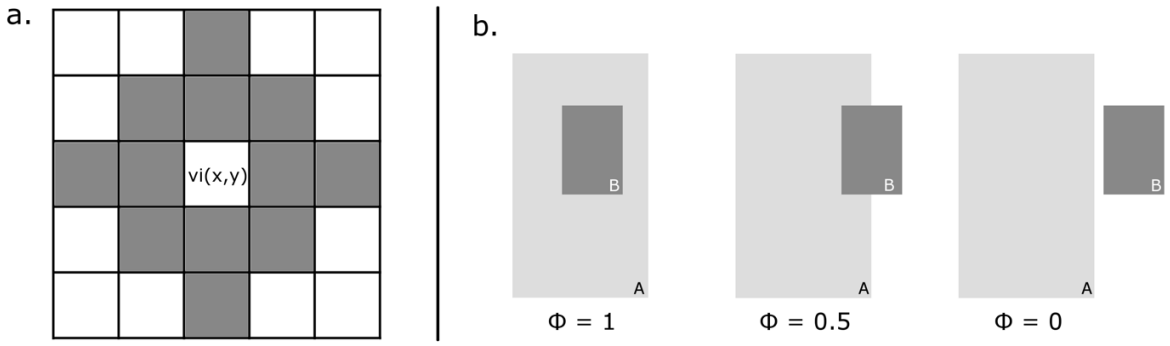

Figure 3: *(a) 12-connected neighboring pattern and (b) Principle of inclusion coefficient of set B in A with 3 examples. (Left) B is totally included in A (Φ = 1), (center) exactly half of set B is out of A (Φ = 0.5), and (right) B is completely out of A (Φ = 0).*

STRG is repeated by incrementing the value of K, starting from K = 1. At each iteration, the average time-intensity curve $S_{avg}^{K}(t)$ of the region R_i^K found by STRG and its feature vector F_{avg}^{K} = [P_m, δ_{max}, AUC, Δt_{max}] are calculated. This algorithm is iterated until it reaches the feature consistency condition as defined in the following:

Lesion segmentation refinement:

Input: R_i input (coarse) segmentation from k-means

λ: consistency coefficient

Outputs: K*: the optimal tolerance threshold,

M_λ : the refined segmentation of R_i

beginning

K ← 0

do

K ← K + 1

R_i^K ← STRG(R_i, K)

$S_{avg}^{K}(t)$ ← mean of $C_i(t)$ of $v_i \in R_i^K$

F_{avg}^{K} ← Compute Features of $S_{avg}^{K}(t)$

while $\left(\frac{\|F_{avg}^{K}\| - \|F_{seed}\|}{\|F_{seed}\|} \leq \lambda\right)$ **AND** $\left(R_i^K < R_n\right)$

$M_\lambda \leftarrow R_i^K$

$K^* \leftarrow K$

End

This finer segmentation M_λ supplies spatial consistency and guarantees time-intensity curve similarity in the region outputted by STRG. Indeed, the neighboring voxels included in the lesion mask are associated with a signal for which the degree of characteristic variation is controlled by the λ criterion.

This algorithm was applied by varying the feature consistency coefficient λ from 0.1 to 0.7 with an incremental value of 0.1. The results were compared with the medical expert segmentation ground-truth masks G considered as a reference by calculating the Dice scores D [17] to determine the optimal value for λ*. λ* was defined as the lower λ value that gave the higher Dice score (equation 10) average over the basal, mid-cavity and apical slices.

$$\lambda^* = arg\max_{\lambda}(Dice(M_\lambda, G)) \quad (10)$$

where M_λ is the segmentation mask processed by automated segmentation. The Dice score is an efficient index that compares the similarity of two segmentations: the proposed segmentation mask M and the ground truth mask G. If the masks perfectly overlap, the Dice score is equal to 1. If masks share no pixels in common, the score is 0. The Dice score is computed as follow (equation 11):

$$Dice(M_\lambda, G) = \frac{2 \cdot (M_\lambda \cap G)}{M_\lambda + G} \quad (11)$$

where |.| means the cardinality of the set and ∩ is the intersection of the two masks. An inclusion coefficient was also calculated from the results computed with STRG and configured with λ = λ*. This criterion is based on medical expert segmentation used as a reference and reflects the automated segmentation mask inclusion in the reference. The inclusion coefficient is established by equation 12:

$$\Phi = \frac{M_{\lambda^*} - M_{\lambda^*} \backslash G}{M_{\lambda^*}} \quad (12)$$

This coefficient calculates the ratio between the surface of M_{λ^*} overlapping with G over the surface of M_{λ^*}. Hence, if M_{λ^*} is completely included in G, then the resulting inclusion criterion is Φ = 1. The score decreases as the surface of M_{λ^*} deviates from mask G until it reaches Φ = 0, when both masks have no common voxels. The principle of this index is represented in Figure 3-b.

We finaly assessed the lesion detection accuracy from the centroid distance. This metric evaluates the distance between the lesion centroids detected by STRG and the ground truth segmentations. The centroid C of a lesion region was computed from equation 13:

$$C = \left(\frac{M_{10}}{M_{00}}, \frac{M_{01}}{M_{00}}\right) \quad (13)$$

where M_{00}, M_{10}, and M_{01}, represent respectively the area, the horizontal moment, and the vertical moment, calculated with equation 14:

$$M_{ij} = \sum_{x=1}^{W} \sum_{y=1}^{H} x^i y^j R(x, y) \quad (14)$$

The distance D between two centroids C_1 and C_2 was then calculated as the Euclidian distance (equation 15).

$$D = \sqrt{((x_{C2} - x_{C1}) - (y_{C2} - y_{C1}))} \quad (15)$$

314

315

316 ***Manual segmentation***

317 Ischemic lesion segmentation was conducted blindly, randomly and independently on a
318 dedicated postprocessing workstation by two level-3 CMR-experienced observers who were
319 unaware of the clinical and angiographic data. The observers were asked to delineate what
320 they would consider the definite ischemic lesion and the remote normal region. They were
321 only allowed to use the original DICOM images for analysis, and lesion segmentation was
322 performed on the frame that was considered the most representative.

323 ***Ground-truth segmentation***

324 Both experts were asked to reach a consensus on the definite ischemic lesion with all available
325 clinical and angiographic data made available to them. They were also allowed to use an
326 interactive spatiotemporal clustering mapping tool to refine their decision based on all
327 spatiotemporal available data. The algorithm of this semi-automated segmentation tool is quite
328 similar to STRG because it allows the user to select a voxel as a seed that is iteratively
329 expanded on its neighbors by matching the condition set by equation (9). In our case, the
330 value of the tolerance threshold was manually set by the user. This final ground-truth
331 segmentation (also known as G) mask set was defined as the reference for subsequent
332 comparisons.

333

Statistical analysis

Data were screened for normality using the Shapiro-Wilk test, and were accordingly reported as the mean ± standard deviation (SD) or median and 95% confidence interval [95% CI]. Using two-way mixed ANOVA modeling, the MBF values were compared among segmentation methods (within-subject factor), with assessment of the main effect and potential interaction of the slice level or type of disease (CAD or microvascular disease) (between-subject factors). Box's conservation correction factor was applied to account for sphericity violation. Posthoc pairwise comparisons were performed when applicable using Bonferroni adjustments.

Statistical analysis was performed using Medcalc 18.2.1 (Ostend, Belgium) and Stata SE 15.1 (Statacorp, College Station, TX, USA). For all analyses, statistical significance was accepted at $p < 0.05$.

Results

Among the 30 included patients, 22 demonstrated focal hypoperfused lesions that were related to macrovascular CAD disease (1-vessel = 9, 2-vessels = 6, 3-vessels = 7), and 8 patients displayed a microvascular diffuse disease (dilated cardiomyopathy = 2, diabetes = 3, hypertrophic cardiomyopathy = 3).

Comparison of MBF values obtained across segmentation approaches

The MBF values obtained after lesion segmentation with the various approaches are shown in Figure 4. Overall, although no main effect of slice location ($p = 0.27$) or disease type ($p = 0.19$) was observed, a significant interaction was noted between disease type and method ($F(5; 410) = 3.55$, $p = 0.004$). A statistically significant difference in mean MBF values was found across methods ($F(5; 415) = 31.24$, $p < 0.001$). Pairwise comparisons showed that although only a minimal and nonsignificant difference was found between the ground-truth reference and STRG (mean difference = 0.02, 95% CI[-0.07, 0.04], $p > 0.9$) or k-means (mean difference = 0.046, 95% CI [-0.1,0.01], $p = 0.24$), significantly higher mean MBF was observed for both manual segmentation (mean difference = 0.14, 95% CI [0.07, 0.2]) and AHA (mean difference = 0.25, 95% CI [0.17, 0.36]).

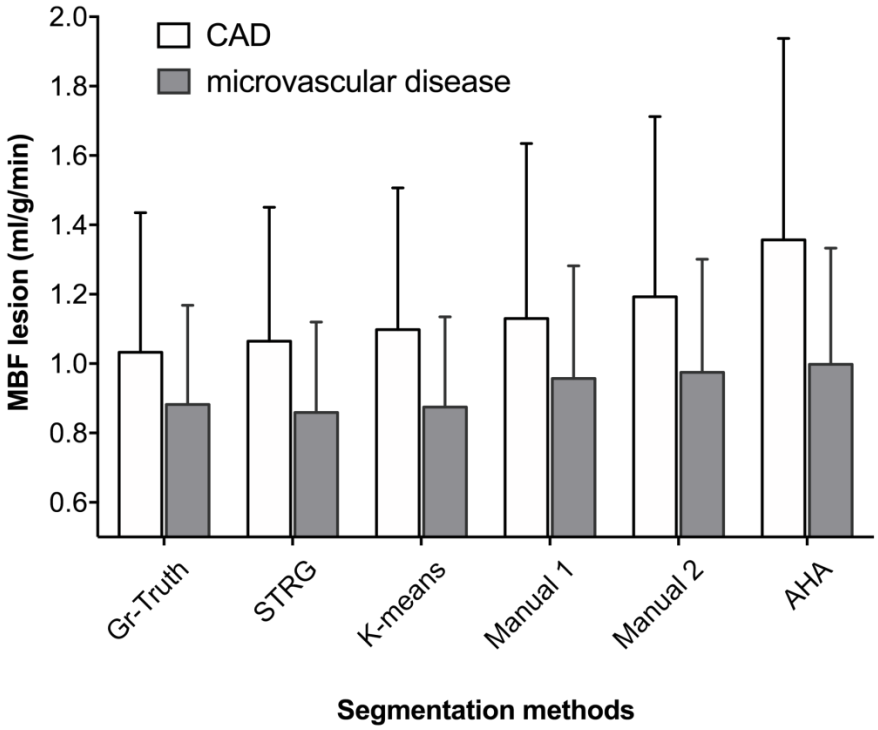

Figure 4*: Average MBF measurements calculated at voxel observation scales in lesions regions detected by ground-truth segmentation defined by a consensus between two medical experts (Gr-Truth), STRG and prior coarse segmentation (STRG and K-means, respectively), manual segmentations performed by the two experts (Manual 1 and Manual 2), and AHA bullseye segmentation (AHA).*

In the lesion regions detected by STRG, we calculated the mean and standard deviation of the blood flows of each MBF measured directly at the voxel scale, $\overline{MBF_{vox}}$ and $SD(MBF_{vox})$, respectively. We compared these with the blood-flow MBF_{ROI} measured on the ROI average-time curve. The median values of the differences observed in the base, middle and apex slices were 20%, 8% and 16% respectively. The standard deviation over the time-intensity curve baseline showed reductions of 58%, 48% and 43% when calculated on the ROI average time curve, hence improving significantly the average time-intensity curve CNR.

Overall, although no main effect of slice location ($p = 0.27$) or disease type ($p = 0.19$) was observed, a significant interaction was noted between disease-type and method ($F(5; 410) = 3.55$, $p = 0.004$). A statistically significant difference in mean MBF values was found across methods ($F(5; 415) = 31.24$, $p < 0.001$). Pairwise comparisons showed that although only a minimal and nonsignificant difference between the ground-truth reference and STRG (mean difference = 0.02, 95% CI[-0.07, 0.04], $p > 0.9$) or k-means (mean difference =

0.046, 95% CI [-0.1,0.01], p = 0.24) occurred, significantly higher mean MBF was observed for both manual segmentation (mean difference = 0.14, 95% CI [0.07, 0.2]) and AHA (mean difference = 0.25, 95% CI [0.17, 0.36]. Such results suggest that STRG is more efficient over the 3 slice levels (base, middle and apex) than the other tested approaches.

When considering the MBF difference between the lesion and the remote region (delta-MBF) in CAD subjects, significant overall differences were found across methods ($F(4; 4236) = 17.43$, $p < 0.001$). No difference in delta-MBF was observed between ground-truth and STRG approaches (mean difference = -0.03, 95% CI[-0.103, 0.040], $p > 0.9$).The delta-MBF was significantly underestimated by manual (m1 $p = 0.004$, m2 $p = 0.02$) and AHA approaches ($p < 0.001$).

Comparison of classifiers using Dice score inclusion coefficient and centroid distance metrics

The median Dice scores calculated for pairs of ground-truth and automatically computed masks M_λ for each value of λ and by slice are listed in Table 1. The first column shows the Dice score reached with the simple k-means preclustering approach masks R. Based on the Dice scores, overall higher patient mask matches were obtained for a coherence coefficient value of $\lambda = 0.5$. Median scores were respectively equal to $D_{base} = 0.62$, $D_{middle} = 0.63$ and $D_{apex} = 0.66$ for base, middle and apical slices. These scores were higher than those obtained with k-means presegmentation ($D_{base} = 0.62$, $D_{middle} = 0.59$ and $D_{apex} = 0.56$, respectively) showing that similarity with the ground-truth mask was better after STRG refinement.

	k-means	**λ = 0.1**	**λ = 0.2**	**λ = 0.3**	**λ = 0.4**	**λ = 0.5**	**λ = 0.6**	**λ = 0.7**
Base	0.62	0.60	0.58	0.62	0.64	0.62	0.65	0.64
Middle	0.59	0.60	0.61	0.63	0.64	0.63	0.63	0.63
Apex	0.56	0.60	0.60	0.60	0.61	0.66	0.63	0.63
Median	0.59	0.60	0.60	0.62	0.63	0.64	0.64	0.63

Table 1: *Median Dice scores among all patients for the three slice levels calculated between expert segmentation masks and k-means clustering (first column), or STRG segmentation masks with λ coefficient values ranging from 0.1 to 0.7. The best Dice score (green column) was obtained for λ= 0.5.*

Tables 2 and 3 report the Dice scores obtained on the same population of patients but divided into two categories: those suffering from focal myocardial lesions (22 patients) and those

suffering from diffuse ischemic diseases (8 patients). The best Dice score for focal lesions was obtained with a slightly higher λ value than for the diffuse lesions. With respect to the relatively low number of patients included in the study and especially when subdivided into subsets, median calculation was chosen instead of average.

	k-means	λ = 0.1	λ = 0.2	λ = 0.3	λ = 0.4	λ = 0.5	λ = 0.6	λ = 0.7
Base	0.62	0.60	0.58	0.66	0.62	0.59	0.64	0.63
Mid	0.59	0.58	0.61	0.63	0.64	0.63	0.67	0.63
Apex	0.59	0.65	0.63	0.66	0.66	0.67	0.67	0.67
Median	0.60	0.61	0.61	0.65	0.64	0.63	0.66	0.64

Table 2: *Median Dice score calculated identically to Table 1, by selecting only the patient sub-population with a focal 1- or 2-vessel disease. The best Dice score (green column) was obtained for λ= 0.6.*

	k-means	λ = 0.1	λ = 0.2	λ = 0.3	λ = 0.4	λ = 0.5	λ = 0.6	λ = 0.7
Base	0.61	0.61	0.56	0.67	0.67	0.67	0.67	0.67
Mid	0.60	0.65	0.60	0.63	0.63	0.62	0.58	0.62
Apex	0.56	0.60	0.60	0.60	0.61	0.66	0.63	0.63
Median	0.59	0.62	0.59	0.63	0.64	0.65	0.63	0.64

Table 3: *Median Dice score calculated identically to Table 1, by selecting only the patient sub-population with diffuse micro-vascular lesions. The best Dice score (green column) was obtained for λ= 0.5 which was the same as for the complete patient population.*

Figure 5 presents the segmentation results from image series acquired on 6 patients suffering from various ischemic lesions. The plots display the average time-intensity curves of the largest regions identified by the final segmentation. In 3 cases (B1, B2 and F1) out of 6, the masks found by the STRG algorithm were more restrictive than the masks found by k-means presegmentation. In all cases and as expected, the average time-intensity curve of the region outputted by STRG $c_{STRG}(t)$ presented a greater peak value enhancement and was smoother than that of $c_{seed}(t)$. When the optimal STRG region M_{λ^*} was more restrictive than the k-means

region R, the behavior of the voxels present in R and outside of M_{λ^*} showed important differences (higher peak value, maximum slope and AUC). This result shows the importance of the refinement supplied by the STRG approach to reach an average signal that is as close as possible to the lesion center without contamination by voxels showing intermediate or low perfusion defects. Oscillations in the time-intensity curves displayed in plot F1 and especially F2 reveal motion correction mismatches. Despite these artifacts, segmentation was accurately detected in both cases.

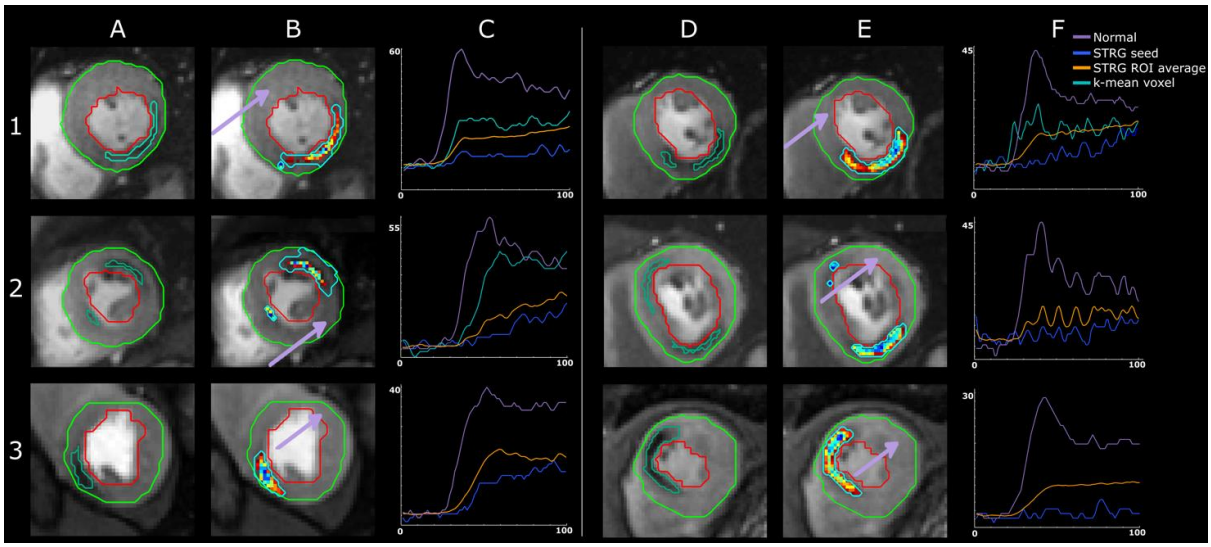

Figure 5: *Segmentation results on mid-ventricular slices acquired in 6 different subjects. Endo and epicardium borders are defined by the red and green contours, respectively. Images on columns A and D expose the manual lesion segmentation. k-means and STRG segmentations are displayed in columns B and E, respectively, with light-blue boundaries and with colored masks. The color map of the STRG mask indicates the threshold value K for which the voxel has been included in the region. The plots in columns C and F show time-intensity curves of: (purple) normal voxels; (light blue) voxels belonging to k-means segmentation and out of the STRG mask (if any); (orange) the STRG mask average; and (dark blue) the STRG seed voxel. Purple arrows indicate the spatial position of the voxel from which was extracted normal signal.*

Table 4 indicates the median and interquartile range (IQR) of inclusion coefficients Φ of STRG segmentation masks M_{λ^*} in the ground-truth masks. These values were calculated over all patient cohorts and over the dense and diffuse patient subsets on basal, middle and apical slices. In the complete patient set, the median (IQR) inclusion coefficients Φ were equal to $\Phi_{base} = 0.68$ (0.30), $\Phi_{middle} = 0.62$ (0.27) and $\Phi_{apex} = 0.75$ (0.30). In comparison, the median (IQR) inclusion coefficients of the k-means segmentation masks R in the ground truth mask were $\Phi_{base} = 0.56$ (0.28), $\Phi_{middle} = 0.56$ (0.22) and $\Phi_{apex} = 0.55$ (0.34). This result indicates that in all cases, inclusion was significantly greater with STRG segmentation than with k-means presegmentation. Table 4 also indicates that the inclusion coefficients are greater on diffuse lesions than on focal ones.

	Base		**Middle**		**Apex**	
	Median	**IQR**	**Median**	**IQR**	**Median**	**IQR**
All patients (λ = 0.5)	0.68	0.30	0.62	0.27	0.75	0.30
focal lesions (λ = 0.6)	0.63	0.30	0.62	0.28	0.74	0.34
Diffuse lesions (λ = 0.5)	0.73	0.23	0.69	0.21	0.76	0.19

Table 4: *Median and interquartile range inclusion coefficients of automated STRG segmentation against expert segmentation, calculated over the entire patient population, focal lesion subset, and diffuse lesion subset. The coefficient was calculated over basal, middle and apical slices.*

		Focal 1- or 2-vessel disease		*Diffuse micro-vascular disease*	
		k-means	***STRG (λ = 0.6)***	***k-means***	***STRG (λ = 0.5)***
Dice Score	**Base**	*0.62(0.20)*	*0.64(0.19)*	*0.61(0.20)*	*0.67(0.16)*
	Middle	*0.59(0.16)*	*0.67(0.14)*	*0.60(0.26)*	*0.62(0.17)*
	Apex	*0.59(0.21)*	*0.67(0.21)*	*0.56(0.18)*	*0.66(0.17)*
Inclusion Coefficient	**Base**	*0.53(0.21)*	*0.63(0.30)*	*0.67(0.48)*	*0.73(0.23)*
	Middle	*0.56(0.25)*	*0.62(0.28)*	*0.57(0.18)*	*0.69(0.21)*
	Apex	*0.58(0.37)*	*0.74(0.34)*	*0.55(0.15)*	*0.76(0.19)*
Centroid Distance (mm)	**Base**	*3.22(2.80)*	*2.54(1.38)*	*2.31(3.45)*	*1.64 (1.44)*
	Middle	*3.15(2.24)*	*2.33(2.81)*	*1.84(1.12)*	*1.73(0.68)*
	Apex	*1.67(1.42)*	*0.97(0.99)*	*3.88(5.51)*	*2.93(1.52)*

Table 5 *: Median (IQR) Dice scores, inclusion coefficients and centroid distances (in mm), calculated over the two patient sub populations for basal, middle and apical slices.*

Table 5 summarizes the medians and interquartile ranges of Dice scores, inclusion coefficients and centroid distances between ground truth and regions detected by k-means and STRG for the two categories of populations. In all cases, the scores were improved by STRG refinement compared to the respective k-means. While the Dice score gave information on the lesion coverage, the centroid distance informed on the location accuracy of the lesion core. Reduction of this distance with the use of STRG, suggests a closer lesion core location to ground truth as defined by experts.

We calculated the median and IQR of the K^* values used in segmentation over the all-patient set and by disease type as defined above (CAD or diffuse diseases) with their respective λ^* values. These values are reported in Table 6 by slice (base, middle and apex). Minor differences were observed between the optimal thresholds used in the context of either CAD of diffuse disease lesion. Nevertheless, in all cases the coefficient IQR calculations indicated a high variability because they ranged from 10.5 to 12. This observation highlights an important amplitude of the used thresholds over all datasets that was independent of the type of lesion and shows that the use of an adaptive threshold was necessary for robust and accurate segmentation.

	Base		Mid		Apex	
	Median	**IQR**	**Median**	**IQR**	**Median**	**IQR**
All patients (λ = 0.5)	8.50	11.5	7	10.5	10.5	12
Focal lesions (λ = 0.6)	8	13	7	13	12	11
Diffuse lesions (λ = 0.5)	10.5	9	11	10	6	14

Table 6*: Median and interquartile range applied threshold K* for STRG segmentation over (line 1) the complete patient population with λ= 0.5, (line 2) the patient population with a focal ischemic lesion and with λ= 0.6, and (line 3) the patient population with diffuse ischemic lesion λ= 0.5*

Principle component analysis

Principle component analysis (PCA) was applied by using the time-intensity curve features extracted from the lesion regions obtained by automated segmentations. PCA was performed to determine selected salient features of the perfusion curves within the different types of segmented lesions. The Pareto diagram in Figure 6 indicates that more than 90% of the information stored in the time-intensity curve features was carried by the first 3 components. For all slices, the first component was essentially based on the peak value and maximum slope, which were highly correlated. The second component was mainly defined by the delay and time-to-peak features. The orthogonality of these features to the maximum slope and peak value suggests independence between the two groups of features. Delay and time to peak were highly correlated in the middle-and apex plot and negatively correlated in the base plot.

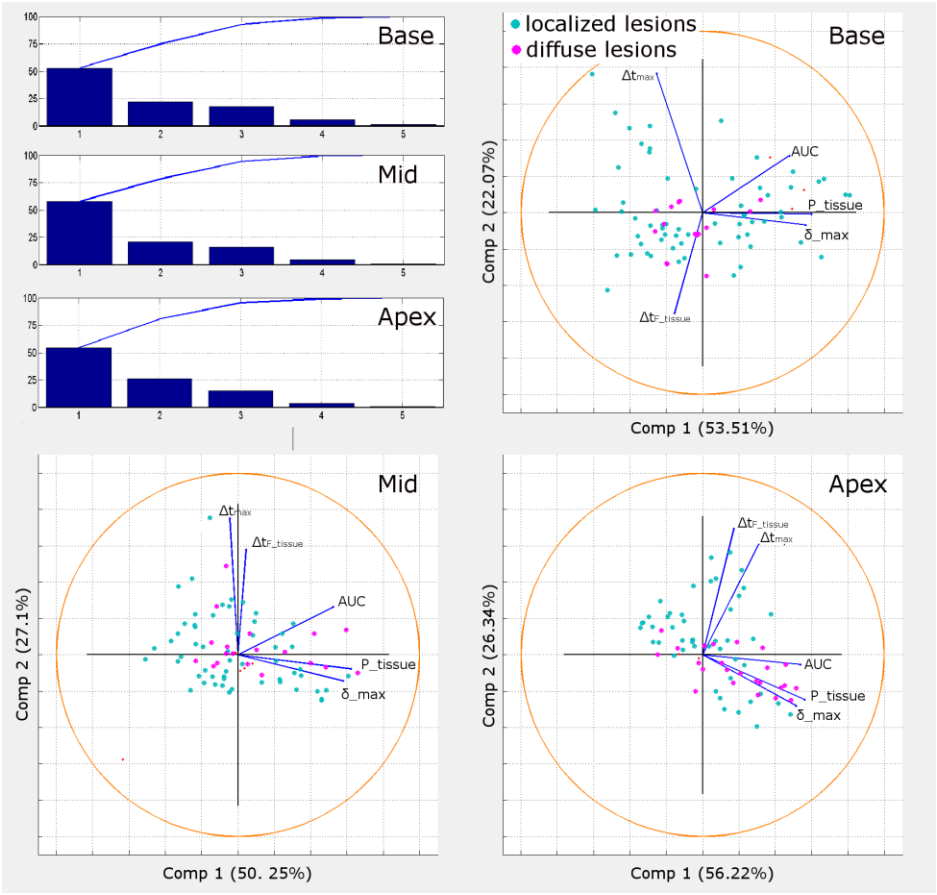

Figure 6: *(top-left) Pareto diagram and principle component analysis plots of average time-intensity curves features in regions automatically segmented by the proposed approach. For ease of visualization, PCA diagrams were plotted over 2 dimensions that already contained more than 75% of the information. Blue points represent focal lesions and magenta diffuse ones.*

The diffuse lesion region signal features appeared to be significantly influenced by the time to peak value and maximum slope feature, especially when examining the apex PCA plot. Focal lesion features were spread over the diagram plot with no significant influence from any feature.

No significant difference between diffuse and focal lesions could be observed. However, it is clear that the diffuse lesion population is more concentrated around the peak value and maximum slope feature vector. This outcome was actually expected because enhancement is more effective in this type of pathology than in focal lesions where the peak value was extremely weak. Hence, the variability could not be determined.

Figure 7 indicates a lesion detected on a patient slice with a focal lesion and aliasing artifact. The presence of this artifact had no impact on the final segmentation due to the use of 3

clusters at the k-means segmentation step. Indeed, a cluster was “sacrificed” for the artifact, but the lesion cluster was sufficiently robust to allow accurate STRG segmentation.

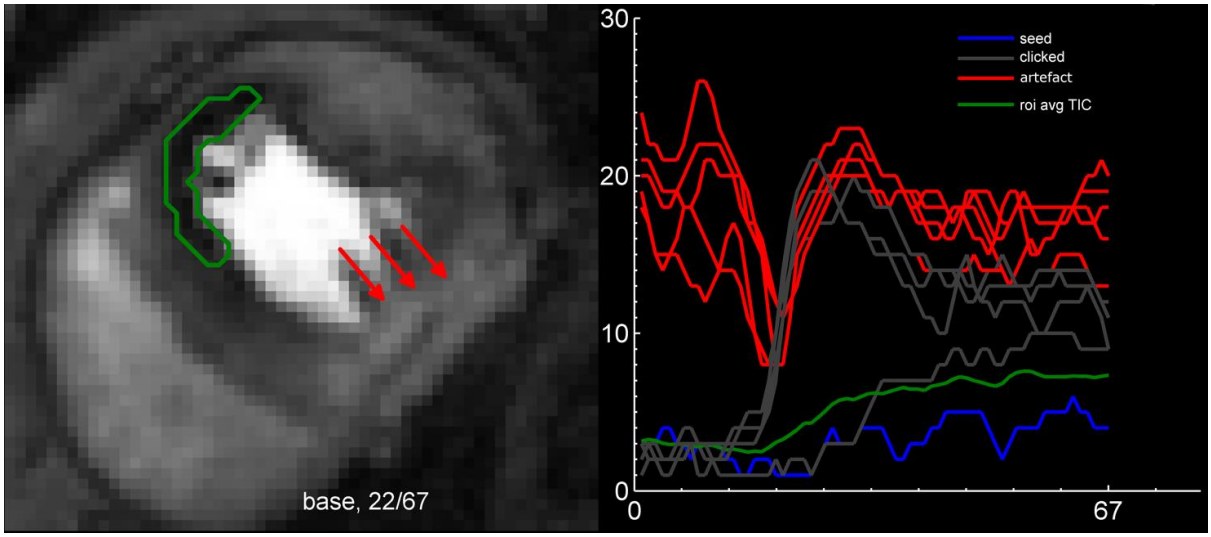

Figure 7: *(left) STRG segmentation result (green) on an image series with aliasing artifact occurring on an inferior segment shown by red arrows; (right) Plots of time-intensity curves of voxels and regions associated with artifact (red) , lesion region detected by STRG (green), lesion region’s seed (blue), voxels out of lesion region (gray).*

Discussion

This proposed segmentation approach offers a robust, easy, reliable and objective automatic method to detect most representative pixels from ischemic coronary lesions using PW images based on the time-intensity curve shapes and features of voxels belonging to the myocardium. Average MBF values measured in targeted lesion regions are indeed lower and closer to the ones obtained by the expert ground-truth classification and have lower standard deviation in the determined region.

Our hierarchical approach proposes a first rough segmentation based on time-intensity curve feature similarity and refinement by a method that sets spatial and temporal constraints regulated by the time-intensity curve features to exploit the totality of the information given by the PW images, especially in the temporal dimension. Exploitation of the spatial constraint only after the second step (STRG) enable multiple lesion detection when it occurs (Figure 5[B2-E2], and Figure 8) since STRG is performed as many times as the number of connected regions detected by k-means clustering.

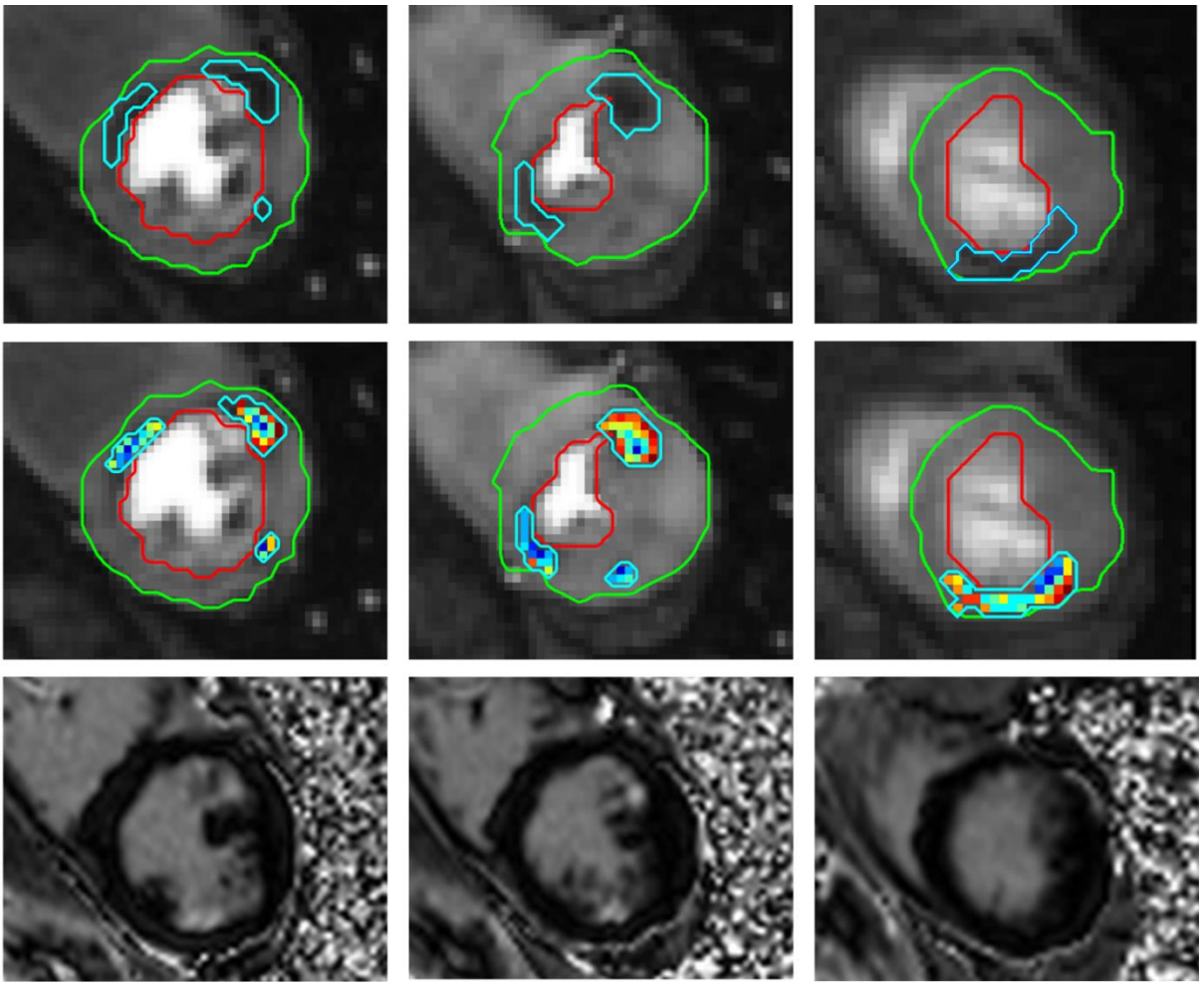

Figure 8: *(top line) Ground-truth segmentation and (middle line) segmentation results on PW-image series at peak enhancement acquired sequentially without delay after the RR wave on a patient with multiple lesions on anterior, septal, and inferolateral segments. Green and red lines indicate the endo and epicardial bounds. k-means (cyan curves) and STRG (color masks) segmentation results totally matched on septal and inferolateral segments. STRG segmentation was slightly more restrictive than k-means on anterior segmentation. (Bottom line) late gadolinium enhancement images acquired on same patient and slices at end-diastole mismatched with perfusion images, indicating pure ischemic lesion without necrosis.*

This method exquisitely considers the high interpatient variability of the signal collected in the images to propose an adaptive method for accurate segmentation. STRG segmentation relies on an automatically set and appropriate tolerance threshold K, based on the average time-intensity curve coherence. This feature gives the method a wide level of flexibility while making it robust to temporal frame coregistration artifacts (Figure 5 – plots F1 and F2) and to aliasing artifacts, as shown in Figure 7.

We observed that measurements of $\overline{MBF_{vox}}$, calculated as an average of MBF values from a map region, showed differences from measurements of MBF_{ROI}, as well as difference from blood flow measurement of the average time curve in the same region. This result shows that in a certain number of cases, there is value in clustering before quantification, even with a simple quantification approach, demonstrating the utility of the segmentation approach.

As shown above by the PCA, the focal ischemic lesions' signal was less homogenous than in the case of diffuse regions, leading to the need for a slightly higher λ value. However, this higher tolerance is compatible with accurate segmentation considering ground-truth comparison because the feature difference between the lesion and healthy tissue is important. In this study, the algorithm was calibrated to obtain the best match between automated and manual segmentations based on the Dice score. Nevertheless, the use of a more restrictive λ-value could guarantee a higher similarity between time-intensity curves and is of interest for analysis of the lesion center because a significant enhancement difference might occur between the time-intensity curves of the seed and final lesion region, as shown in Figure 5, plot F3.

By showing that lesion feature variability was important, especially for focal lesions, PCA also confirmed that an accurate and robust segmentation cannot only consider one feature, but a combination of features, done in this study.

Nevertheless, this technique presents one limitation. This technique relies on the exploitation of relative differences between time-intensity curve features regardless of any analysis of the

meaning of these quantities. As a consequence, this method cannot be considered solely for triage between healthy and CAD patients.

In all contexts, the Dice score reached a modest value although the results met visual agreement. We note that the Dice score, which is a common and frequently used comparison method, is intrinsically not the best approach for evaluating such results. Indeed, if physicians are trained to detect the culprit sectors with high sensitivity, they never precisely size the ischemic lesions and only the voxels with minimal doubt are conserved for the ground-truth definition. Moreover, although the Dice score is highly dependent on the lesion size, the spatial surface of the smallest lesions can be less than 10 voxels. In this particular case, small variations between detection and ground-truth might lead to important reduction of the score. Therefore, our proposed method could perhaps be considered as more invariant and reliable than subjective manual segmentation.

The Dice score was complemented by inclusion coefficient Φ, and centroid distance. The first showed the segmentation accuracy of STRG with a median ranging between $\Phi = 0.62$ and $\Phi = 0.76$. Hence, a major portion of the STRG segmentation mask M_{λ^*} was similar to the ground-truth mask, but a portion of this latter group was somehow rejected by STRG because the time-intensity curve behavior of this portion of the surface did not match the seed signal under the conditions laid down by the consistency coefficient λ^*. This result suggests that the STRG segmentation was more restrictive than that performed by the clinician in charge of reference segmentation. This restrictive segmentation is nevertheless crucial because the behavior of the average region time-intensity curve must reflect the microcirculation of the segmented region particularly, in the case of the perfusion indexes measurement context in which the quantification approaches are often ill-conditioned problems and rely on assumptions required to isolate a solution. The centroid distance showed the improvement of lesion center location accuracy when STRG was applied compared to k-means. In other words, STRG also modifies the k-means presegmentation to “refocus“ the lesion core because STRG can very accurately detect the location of the seed that is the voxel showing the lowest indicator uptake. The lesion region is then built around this seed by aggregating adjacent voxels matching the initial curve behavior. It is therefore not surprising that STRG improves centroid distance score.

Even if these metrics allowed us to highlight spatial differences, only the MBF variability should be considered to evaluate the approach accuracy. The reason is mainly the difficulty of defining a robust and precise delineation of the lesion because the temporal dimension acquired image series makes it difficult to make an incontestable lesion region definition. Indeed, only one frame of the series – often the peak contrast frame - is used, due to the

representation limitation, when the perfusion defect information is spread over the entire series.

We also emphasize that this segmentation technique used AIF calculated from LR-SRT images to improve the robustness of the myocardium TIC features in the FR-LRT images. The LR-SRT images are usually exploited, as in this work, for perfusion quantification purposes because they allow avoidance of the signal distortions in the LV blood pool due to important contrast agent concentration [11]. However, the CNR from the LV blood pool signal of the FR-LRT images could be sufficient to perform accurate myocardium $S_t(t)$ feature extraction. Hence, we anticipate no difficulty in adapting the pipeline approach with PW images acquired using other techniques, as long as they supply a sufficient CNR.

This segmentation technique proved its ability to yield robust and accurate lesion segmentation results with the use of only semiquantitative perfusion parameters. This approach also guarantees time-intensity curve homogeneity by constraining the variation of features by a single coefficient. Moreover, this approach could be combined with prior segmentation via a myocardium segmentation technique. Further work should be performed to tackle this issue by using convolutional neural networks.

The use of complex perfusion models for perfusion indexes quantification is often limited because it requires assumptions that are difficult to make, due to a lack of knowledge of the physiological mechanisms in the lesion, and in particular, at the voxel observation scale level. The average time-intensity curve regions where the homogeneity of microcirculation behavior is guaranteed could offer possibilities for assumptions by analysis of its shape where implementation would be far too long if this analysis would have to be done voxel by voxel. Associated with LSI deconvolution methods, this approach can supply regions with attenuated breathing and heart movement artifacts, and improve CNR in lesion locations where it is particularly low. Hence, the accuracy and robustness of measurements could be improved.

From the perspective of improvements, this study did not exploit the spatial inter-slice lesion detection coherence to enhance the algorithm's robustness. However, this information, which is widely used by clinicians, could be a good indicator to eliminate casual false positive detection. Moreover, according to recent advances in segmentation based on machine learning approaches, the manually performed myocardium segmentation on FR-LRT images should soon be performed automatically with acceptable robustness [18–21], even in ischemic patients.

In conclusion, the approach proposed in this work aimed to aggregate the voxels most likely belonging to ischemic lesions. This classification was compared with the ground truth selection

performed by two experts. Our study demonstrated that this approach automatically achieved the closest ground truth clustering of voxels belonging to the lesion, provided that at least one lesion exists, which is the only limitation of the developed solution. To our knowledge, there are no large clinical studies that permit us to clearly understand how MBF values are spread between different patient groups clustered by their pathologies. We could legitimately consider that a large-scale descriptive statistic could be used to characterize normal values and thus introduce additional characteristics such as normal value limits, perhaps concluding that MBF values are normal in the absence of lesions.

The output of our algorithm can be directly applied for inline calculation of the MBF in the determined culprit region of interest to supply i) automatic and robust detection of the culprit sector(s) that intrinsically excludes susceptibility artifacts and ii) the most representative stress MBF values in the suspected regions. Indeed, stress MBF are as the most clinically relevant parameter for clinical decision-making prior to revascularization [22].

Appendix

Figure A-1: Arterial input function extraction process. The AIF is extracted from (a) the LR-SRT image series by segmentation (light blue surface) of the LV blood pool cavity (b) Time-intensity curves of voxels owning to this region are then analyzed to identify the one (light yellow) reaching the highest peak value. This value is set as the peak reference P_{ref}, and (yellow) voxels v_a whose peak values reaching more than 80% of P_{ref} are considered as relevant for the AIF estimation. The (green) AIF time-intensity curve $S_a(t)$ is then calculated as the average time-intensity curves $c_a(t)$ of voxels v_a.

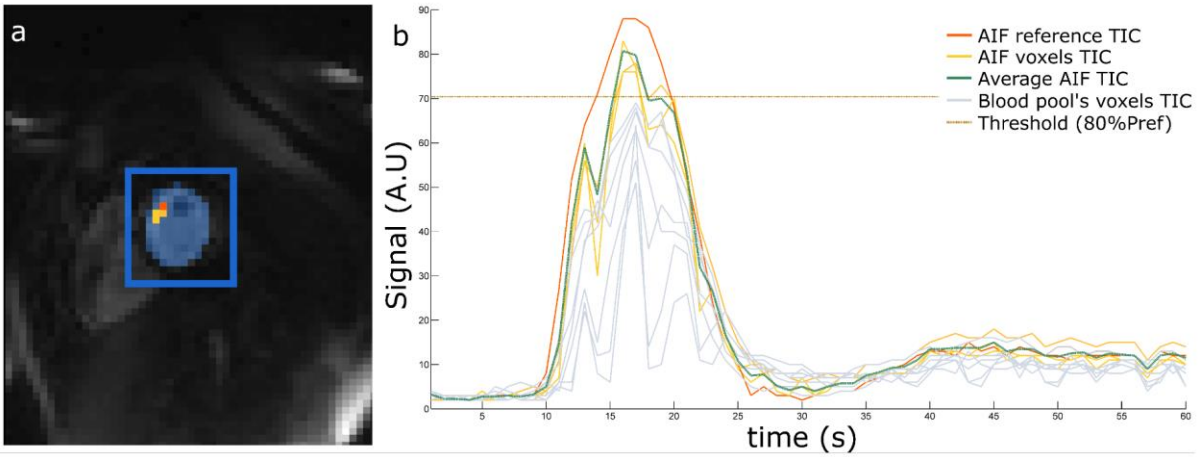

Acknowledgments:

This work was supported by the LABEX PRIMES (ANR-11-LABX-0063) of Université de Lyon, within the program "Investissements d'Avenir" (ANR-11-IDEX-0007) operated by the French National Research Agency (ANR).

This work was supported by the RHU MARVELOUS (ANR-16-RHUS-0009) of l'Université Claude Bernard Lyon 1 (UCBL), within the program "Investissements d'Avenir" operated by the French National Research Agency (ANR).

This work was performed on a platform / by a laboratory member of France Life Imaging network (grant ANR-11-INBS-0006)

References

[1] K.L. Gould, N.P. Johnson, T.M. Bateman, R.S. Beanlands, F.M. Bengel, R. Bober, P.G. Camici, M.D. Cerqueira, B.J.W. Chow, M.F. Di Carli, S. Dorbala, H. Gewirtz, R.J. Gropler, P.A. Kaufmann, P. Knaapen, J. Knuuti, M.E. Merhige, K.P. Rentrop, T.D. Ruddy, H.R. Schelbert, T.H. Schindler, M. Schwaiger, S. Sdringola, J. Vitarello, K.A. Williams, D. Gordon, V. Dilsizian, J. Narula, Anatomic Versus Physiologic Assessment of Coronary Artery Disease, J. Am. Coll. Cardiol. 62 (2013) 1639–1653. doi:10.1016/j.jacc.2013.07.076.

[2] D.C. Lee, N.P. Johnson, Quantification of Absolute Myocardial Blood Flow by Magnetic Resonance Perfusion Imaging, JACC-Cardiovasc. Imag. 2 (2009) 761–770. doi:10.1016/j.jcmg.2009.04.003.

[3] M. Jerosch-Herold, Quantification of myocardial perfusion by cardiovascular magnetic resonance, J. Cardiov. Magn. Reson. 12 (2010) 57. doi:10.1186/1532-429X-12-57.

[4] M. Li, T. Zhou, L. Yang, Z. Peng, J. Ding, G. Sun, Diagnostic accuracy of myocardial magnetic resonance perfusion to diagnose ischemic stenosis with fractional flow reserve as reference: systematic review and meta-analysis, JACC Cardiovasc Imaging. 7 (2014) 1098–1105. doi:10.1016/j.jcmg.2014.07.011.

[5] J.P. Greenwood, N. Maredia, J.F. Younger, J.M. Brown, J. Nixon, C.C. Everett, P. Bijsterveld, J.P. Ridgway, A. Radjenovic, C.J. Dickinson, S.G. Ball, S. Plein, Cardiovascular magnetic resonance and single-photon emission computed tomography for diagnosis of coronary heart disease (CE-MARC): a prospective trial, Lancet. 379 (2012) 453–460. doi:10.1016/S0140-6736(11)61335-4.

[6] K. Kudo, S. Christensen, M. Sasaki, L. Østergaard, H. Shirato, K. Ogasawara, M. Wintermark, S. Warach, Stroke Imaging Repository (STIR) Investigators, Accuracy and reliability assessment of CT and MR perfusion analysis software using a digital phantom, Radiology. 267 (2013) 201–211. doi:10.1148/radiol.12112618.

[7] S.P. Sourbron, D.L. Buckley, Tracer kinetic modelling in MRI: estimating perfusion and capillary permeability, Phys. Med. Biol. 57 (2012) R1–R33. doi:10.1088/0031-9155/57/2/R1.

[8] M.D. Cerqueira, N.J. Weissman, V. Dilsizian, A.K. Jacobs, S. Kaul, W.K. Laskey, D.J. Pennell, J.A. Rumberger, T. Ryan, M.S. Verani, American Heart Association Writing Group on Myocardial Segmentation and Registration for Cardiac Imaging, Standardized myocardial segmentation and nomenclature for tomographic imaging of the heart. A statement for healthcare professionals from the Cardiac Imaging Committee of the Council on Clinical Cardiology of the American Heart Association, Int J Cardiovasc Imaging. 18 (2002) 539–542.

[9] T.F. Ismail, L.-Y. Hsu, A.M. Greve, C. Goncalves, A. Jabbour, A. Gulati, B. Hewins, N. Mistry, R. Wage, M. Roughton, P.F. Ferreira, P. Gatehouse, D. Firmin, R. O'Hanlon, D.J. Pennell, S.K. Prasad, A.E. Arai, Coronary microvascular ischemia in hypertrophic cardiomyopathy - a pixel-wise quantitative cardiovascular magnetic resonance perfusion study, J. Cardiov. Magn. Reson. 16 (2014) 49. doi:10.1186/s12968-014-0049-1.

[10] T. Chitiboi, A. Hennemuth, L. Tautz, P. Stolzmann, O.F. Donati, L. Linsen, H.K. Hahn, Automatic Detection of Myocardial Perfusion Defects using Object-based Myocardium Segmentation, in: 2013 Computing in Cardiology Conference (Cinc), Ieee, New York, 2013: pp. 639–642.

[11] P.D. Gatehouse, A.G. Elkington, N.A. Ablitt, G.-Z. Yang, D.J. Pennell, D.N. Firmin, Accurate assessment of the arterial input function during high-dose myocardial perfusion cardiovascular magnetic resonance, J Magn Reson Imaging. 20 (2004) 39–45. doi:10.1002/jmri.20054.

[12] H. Xue, J. Guehring, L. Srinivasan, S. Zuehlsdorff, K. Saddi, C. Chefdhotel, J.V. Hajnal, D. Rueckert, Evaluation of Rigid and Non-rigid Motion Compensation of Cardiac Perfusion MRI, in: D. Metaxas, L. Axel, G. Fichtinger, G. Szekely (Eds.), Medical Image

Computing and Computer-Assisted Intervention - Miccai 2008, Pt Ii, Proceedings, Springer-Verlag Berlin, Berlin, 2008: pp. 35–43.
[13] R.W.M. Underberg, F.J. Lagerwaard, B.J. Slotman, J.P. Cuijpers, S. Senan, Use of maximum intensity projections (MIP) for target volume generation in 4DCT scans for lung cancer, Int. J. Radiat. Oncol. Biol. Phys. 63 (2005) 253–260. doi:10.1016/j.ijrobp.2005.05.045.
[14] M.S. Hansen, H. Olafsdottir, K. Sjostrand, S.G. Erbou, M.B. Stegmann, H.B.W. Larsson, R. Larsen, Ischemic segment detection using the support vector domain description, in: J.P.W. Pluim, J.M. Reinhardt (Eds.), Medical Imaging 2007: Image Processing, Pts 1-3, Spie-Int Soc Optical Engineering, Bellingham, 2007: p. UNSP 65120F.
[15] S. Lloyd, Least-Squares Quantization in Pcm, IEEE Trans. Inf. Theory. 28 (1982) 129–137. doi:10.1109/TIT.1982.1056489.
[16] D. Arthur, S. Vassilvitskii, k-means plus plus : The Advantages of Careful Seeding, Siam, Philadelphia, 2007.
[17] Lee Raymond Dice, Measures of the Amount of Ecologic Association Between Species, Ecology. 26 (1945) 297–302.
[18] M.R. Avendi, A. Kheradvar, H. Jafarkhani, A combined deep-learning and deformable-model approach to fully automatic segmentation of the left ventricle in cardiac MRI, Med. Image Anal. 30 (2016) 108–119. doi:10.1016/j.media.2016.01.005.
[19] X. Alba, K. Lekadir, M. Pereanez, P. Medrano-Gracia, A.A. Young, A.F. Frangi, Automatic initialization and quality control of large-scale cardiac MRI segmentations, Med. Image Anal. 43 (2018) 129–141. doi:10.1016/j.media.2017.10.001.
[20] A.H. Curiale, F.D. Colavecchia, P. Kaluza, R.A. Isoardi, G. Mato, Automatic Myocardial Segmentation by Using A Deep Learning Network in Cardiac MRI, Ieee, New York, 2017.
[21] P.V. Tran, A Fully Convolutional Neural Network for Cardiac Segmentation in Short-Axis MRI, CoRR. abs/1604.00494 (2016).
[22] J. Schwitter, C.M. Wacker, N. Wilke, N. Al-Saadi, E. Sauer, K. Huettle, S.O. Schönberg, A. Luchner, O. Strohm, H. Ahlstrom, T. Dill, N. Hoebel, T. Simor, MR-IMPACT II: Magnetic Resonance Imaging for Myocardial Perfusion Assessment in Coronary artery disease Trial: perfusion-cardiac magnetic resonance vs. single-photon emission computed tomography for the detection of coronary artery disease: a comparative multicentre, multivendor trial, Eur Heart J. 34 (2013) 775–781. doi:10.1093/eurheartj/ehs022.